JOURNAL OF GEOPHYSICAL RESEARCH, VOL. 101, NO. D14, PAGES 19,237–19,244, AUGUST 27, 1996

Modeling of particle size distribution and its influence on the radiative properties of mineral dust aerosol

Ina Tegen

Department of Applied Physics, Columbia University, New York

Andrew A. Lacis

NASA Goddard Institute for Space Studies, New York

Abstract. The radiative parameters of mineral aerosols are strongly dependent on particle size. Therefore explicit modeling of particle size distribution is needed to calculate the radiative effects and the climate impact of mineral dust. We describe a parameterization of the global mineral aerosol size distribution in a transport model using eight size classes between 0.1 and 10 μm. The model prescribes the initial size distribution using soil texture data and aerosol size measurements close to the ground. During transport, the size distribution changes as larger particles settle out faster than smaller particles. Results of Mie scattering calculations of radiative parameters (extinction efficiency, single scattering albedo, asymmetry parameter) of mineral dust are shown at wavelengths between 0.3 and 30 μm for effective particle radii between 0.1 and 10 μm. Also included are radiative properties (reflection, absorption, transmission) calculated for a dust optical thickness of 0.1. Preliminary studies with the Goddard Institute for Space Studies (GISS) general circulation model (GCM), using two particle size modes, show regional changes in radiative flux at the top of the atmosphere as large as $+15\,\mathrm{W\,m^{-2}}$ at solar and $+5\,\mathrm{W\,m^{-2}}$ at thermal wavelengths in the annual mean, indicating that dust forcing is an important factor in the global radiation budget.

1. Introduction

The radiative effect and climate impact of aerosols is one of the largest uncertainties in modeling the radiative forcing of climate change. So far no systematic assessment of the climate impact of mineral dust aerosol has been carried out, although in many regions desert dust contributes the major part of the aerosol mass loading, occasionally producing prominent features in satellite optical thickness retrievals [*Rao et al.*, 1988]. Owing to frequent occurences of high mass loading and optical thicknesses, mineral dust aerosol can be expected to influence local climate features, as well as the global radiation budget. As dust loading in the atmosphere is highly variable in space and time, its actual distribution is difficult to quantify. A global transport model [*Tegen and Fung*, 1994] can be used to effectively describe the seasonal and geographic changes in global dust distributions.

Radiative impact of aerosols depends not only on aerosol concentration in space and time but also on their size distribution and chemical composition. Compared to anthropogenic sulfate and volcanic aerosol, desert dust is generally larger in size and more absorbing at solar wavelengths. This results in increased atmospheric heating in the presence of dust along with decreased incident solar radiation at the ground and some greenhouse trapping of outgoing thermal radiation. Therefore to accurately determine the combined effects on solar and thermal radiation, explicit calculations of radiative transfer are necessary.

As shown in previous general circulation model (GCM) simulations [*Coakley and Cess*, 1985; *Tegen and Lacis*, 1994], the principal radiative effect of mineral dust aerosol is to heat the atmosphere, with the maximum heating occuring in source regions. Locally, this could inhibit convection and reduce cloud cover and precipitation. Thus for realistic GCM simulations of mineral dust, the radiative effects of the particle size distribution, as well as the space-time distribution of dust concentrations, must be explicitly included in the model calculations.

2. Mineral Dust Transport Model

To determine the spatial and temporal distribution of desert dust, including particle size information, we begin with a source and sink parameterization for desert dust described by *Tegen and Fung* [1994]. In the Goddard Institute for Space Studies (GISS) tracer model,

Paper number 95JD03610.
0148-0227/96/95JD-03610$09.00

dust deflation can occur wherever the soil is dry and the vegetation is low and sparse. We assume dust mobilization to be possible when the soil matric potential is higher than 10^4 J/kg, using monthly mean soil water contents as derived by *Bouwman et al.* [1993]. We use the vegetation data set of *Matthews* [1983] to extract areas where the vegetation cover allows dust uplift, such as deserts, grassland, and shrub land. The amount of uplifted dust approximately follows $q_a = C(u - u_{tr})u^2$ [*Gillette,* 1978], where q_a is the dust flux from the surface, u is the surface wind speed, and u_{tr} is a threshold velocity.

We chose a threshold velocity of $6.5\,\mathrm{m\,s^{-1}}$ at 10–m height, corresponding to *Kalma et al.* [1988]. Since high–resolution wind data are required for these calculations, we used the European Center for Medium Range Weather Forecasts (ECMWF) wind products (10–m surface winds) with a spatial resolution of 1.125° × 1.125° and 6–hour time resolution. Removal of dust by wet deposition was parameterized using climatological precipitation data [*Shea,* 1986]. Dry deposition was described by gravitational settling and turbulent mixing as done by *Genthon* [1992]. The dust transport in the atmosphere was calculated using the three–dimensional GISS tracer model (8° × 10° horizontal resolution, nine vertical atmospheric layers) [e.g., *Prather et al.,* 1987; *Fung et al.,* 1983], where source and sink terms were included.

Soil particle size distributions were derived from the 1° × 1° data set of soil types and particle sizes [*Zobler,* 1986], where the fractions of three major size classes are given as percentages of total soil mass in each grid box. The size classes are sand (particle radius larger than 25 μm), silt (particle radius between 1 and 25 μm), and clay (particles smaller than 1 μm). Since the atmospheric lifetime of particles larger than 10 μm is less than a day, only particles smaller than 10 μm need to be considered for calculations of dust radiative effects. For each size fraction the model calculates deflation, transport, and deposition. In our model, particles from different size classes do not interact with each other. The physical mechanism that affects the different particle size classes in the model is gravitational settling, as larger particles have shorter atmospheric lifetimes due to their higher sedimentation velocity.

3. Optical Thickness and Radiative Properties of Dust

Dust mass loading and optical thickness are related by

$$M = \frac{4}{3}\rho r \tau Q_{ext}^{-1} \tag{1}$$

where M is the column mass loading for each size class, ρ is the particle mass density, r is the effective radius (cross–section weighted radius over the size distribution [*Hansen and Travis,* 1974]), τ is the aerosol optical depth at the reference wavelength $\lambda = 0.55\,\mu$m, and Q_{ext} is the Mie scattering extinction efficiency factor also referenced at $\lambda = 0.55\,\mu$m. The radiative parameters for wind–blown dust were calculated using the Mie scattering theory and the standard gamma size distribution with effective variance of 0.2 for each size bin for refractive indices reported by *Volz* [1973] and *Patterson et al.* [1977]. Measurements of refractive indices for wavelengths between 0.3 and 30 μm are available for for far-traveled Saharan dust. Dust from other regions, like Asia or Australia may have different refractive indices which could lead to uncertainties in the radiative flux computations in those areas.

While dust particles are known to be nonspherical with aspect ratios of the order of 1.7 [*Nakajima et al.,* 1989], Mie scattering calculations can, nevertheless, be used to compute the effective radiative parameters for equivalent volume spheres when the application is radiative forcing computation. Nonspherical effects are important in remote sensing applications, as for example, when computing aerosol optical depths from measurements of bidirectional intensities. However, in the calculation of radiative fluxes and albedos (where spherical/nonspherical differences disappear in the angular integration), Mie scattering parameters calculated for equivalent volume spheres provide very good representation for nonspherical particle scattering. This has been shown by detailed T-matrix calculations for randomly oriented spheroids [*Mishchenko,* 1993; *Mishchenko and Travis,* 1994; *Lacis and Mishchenko,* 1995].

Figure 1 shows the results of Mie scattering calculations for the spectral dependence of dust optical parameters and their progressive change with particle size. The refractive indices used are from *Patterson et al.* [1977] and *Volz* [1973]. Since the size spectrum of desert dust varies considerably depending on prevailing weather conditions [*d'Almeida,* 1987], we have selected a size range from 0.1 to 10 μm. The extinction efficiency factors Q_{ext} (which is the average extinction cross section divided by the geometric cross-sectional area of the particle), are shown normalized to unity at the reference wavelength $\lambda = 0.55\,\mu$m (with the actual extinction efficiencies given in Table 1). Also shown is the single scattering albedo, ω_0 (which is the ratio of scattering optical thickness to extinction optical thickness), and asymmetry parameter g (which is the weighted mean of the cosine of the scattering angle). The Mie scattering calculations are made using the standard gamma size distribution with an effective variance of 0.2 [*Hansen and Travis,* 1974] for sizes spanning the dust size spectrum. The spectral range from 0.3 to 30 μm covers the solar and thermal regimes with 3 μm as the approximate dividing line. To note is the strong dependence on particle size of the extinction efficiency at solar wavelengths for submicron particles, the decrease in single scattering albedo with particle size at solar wavelengths, and the increase in extinction efficiency at thermal wavelengths for the larger particle sizes.

To express the spectral dependence of dust optical properties in terms of their radiative properties, we have inserted the optical parameters from Figure 1 into a radiative transfer model [*Lacis and Hansen,* 1974] to cal-

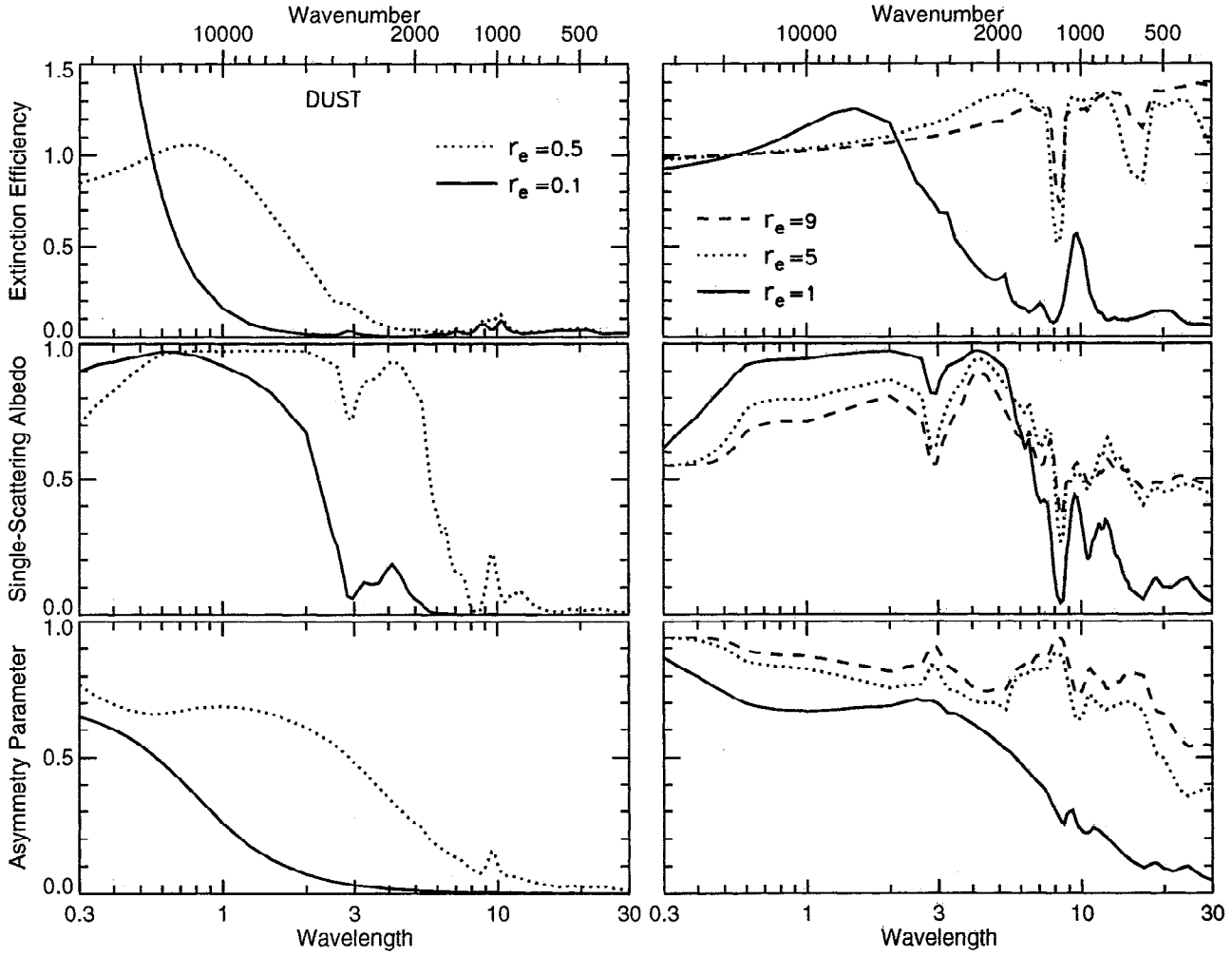

Figure 1. Mie scattering calculated radiative parameters for desert dust aerosol for eight particle sizes (effective radii, r_e, given in micrometers) in dependence on wavelength (in micrometers).

culate the reflection, transmission, and absorption dependence for an isolated aerosol layer of optical depth of $\tau = 0.1$ (Figure 2). The calculated results re-emphasize the strong dependences of the radiative properties of dust on particle size, ranging from mostly reflecting at solar wavelengths ($r = 0.15\,\mu$m) to strongly absorbing for the larger particles ($r = 8\,\mu$m) with increasing absorption at thermal wavelengths. Thus it is clear that a multicomponent size distribution is required to model the full radiative effects of dust aerosols.

4. Modeling of Particle Size Distributions

According to the results of the radiation calculation, the "clay" and "small silt" fractions were each subdivided into four smaller size categories as shown in Table 1. The chosen size classes represent area-weighted effective radii and atmospheric lifetimes calculated by the transport model. For the submicron clay particles, the mean atmospheric lifetimes calculated by our transport model range between 219 hours for $0.8\,\mu$m particles and 231 hours for $0.15\,\mu$m particles, indicating that for these particle sizes the atmospheric lifetime is not determined by gravitational settling but rather by wet deposition and turbulent mixing. For silt particles, however, gravitational settling is the dominant removal mechanism. The lifetimes of silt range from 179 hours for $1.5\,\mu$m particles to 28 hours for $8\,\mu$m particles.

The source distribution of particle sizes used in the transport model is shown in Figure 3 for the eight particle size classes. This size distribution represents the soil particles that are available for deflation. As smaller clay particles tend to agglomerate and stick to larger particles, this leads to a decreased availability of small clay particles for wind erosion [*Scheffer and Schachtschabel*, 1992]. The mass size distribution of dust is shown in relative units. For comparison, measurements of mass size distributions of mineral dust aerosol in source regions are also shown. Dust samples for size measurements are usually taken several meters above the surface. Because of their long atmospheric lifetimes (Table 1), the size distribution of particles smaller than $1\,\mu$m does not change appreciably during transport over short distances. Therefore in the case of clay-sized particles, the measured size distributions are likely to reflect the initial source distribution and thus were chosen to fit the observed size distribution.

Compared to clay-sized particles, silt particles have considerably shorter atmospheric lifetimes. Several meters above the surface (where dust samples are usually collected) the relative concentration of larger particles may already be depleted relative to their initial source distribution because of their high sedimentation velocity. For this reason the exact form of the initial size distribution of silt is not relevant and a simple lognormal distribution ($dM/d\log r$ = const) was chosen as initial size distribution for the silt fraction for particle sizes $1 < r < 10\,\mu$m.

During transport, the dust size distribution changes as larger particles settle out faster than smaller particles. Figure 4 shows model derived mass size distributions of mineral dust in three model layers at pressure levels of 950, 470, and 40 mbar in the global and annual mean. We see that with increasing height, not only does the dust concentration decrease with height but also the maximum in the size distribution shifts from about $1.5\,\mu$m to about $0.8\,\mu$m as larger particles are removed by gravitational settling before they can reach higher atmospheric layers.

Table 1 summarizes the mean atmospheric lifetimes, the annual source strengths, the mean column mass load, the extinction factors Q_{ext} referenced at a wavelength of $0.55\,\mu$m, and the resulting optical thicknesses also referenced at $0.55\,\mu$m for the eight dust size classes. The numbers for global mean mass loading show that particles larger than $1.8\,\mu$m contribute only about 20% to the total dust mass loading, while this size fraction contributes about 60% to the total source strength for particles in the size range between 0.1 and $10\,\mu$m. Particles larger than $1.8\,\mu$m contribute only about 4% to the mean optical thickness, as τ decreases with increasing particle radius for a given mass load. Particles in the radius range between 6 and $10\,\mu$m contribute only 0.2% to the mean optical thickness. This supports our omission of particles larger than $10\,\mu$m from consideration in the dust model as their radiative effect is negligible, although their source strengths may be significant. While about 60% of the modeled dust mass loading is caused by particles in the size range of 0.6 to $1.8\,\mu$m, about 60% of the optical thickness is caused by particles in the range of 0.3 to $1\,\mu$m.

The above approach in describing size distributions has the advantage of enabling dynamic modeling of changes in particle size distribution due to gravitational settling. Figure 5 shows the modeled annual mean optical thickness at $0.55\,\mu$m for the combined eight particle size fractions of the desert dust aerosol integrated over all vertical layers. The results are in good agreement with the advanced very high resolution radiometer (AVHRR) observed optical thickness retrievals [*Rao et al.*, 1988]. The maximum calculated optical thickness is 0.5 over Saudi Arabia in July, the global annual mean desert dust optical thickness is 0.03.

Table 1. Model Results

Size Range, μm	Effective Radius, μm	Lifetime, hours	Source Strength, Mt yr^{-1}	Mass Loading, mg m^{-2}	Mass Loading, Percent	$Q_{ext}(0.55)$	τ, 10^{-3}	τ, Percent
0.1–0.18	0.15	231	2	0.2	0.5	1.536	0.6	2
0.18–0.3	0.25	229	18	1.5	4	2.816	5.1	15
0.3–0.6	0.4	225	52	4.2	12	3.086	9.8	29
0.6–1	0.8	219	150	11.5	31	2.583	11.1	33
1–1.8	1.5	179	250	11.9	32	2.345	5.3	15
1.8–3	2.5	126	250	4.6	13	2.240	1.2	3
3–6	4	67	250	1.8	5	2.174	0.3	0.8
6–10	8	28	250	0.9	2	2.110	0.06	0.2

Table shows results for global mean atmospheric lifetime, annual source strenghts, global annual mean column mass loading, extinction factor Q_{ext} at a wavelength of $0.55\,\mu$m, and global annual mean optical thickness τ at a wavelength of $0.55\,\mu$m for the eight size classes of mineral aerosol between 0.1 and $10\,\mu$m. Column mass loading and optical thickness values for the individual size classes are given in absolute numbers and in percent of the sum over all size classes.

5. Radiative Effect of Dust

Figure 6 shows the net change in radiative flux at the tropopause caused by dust aerosol of optical thickness

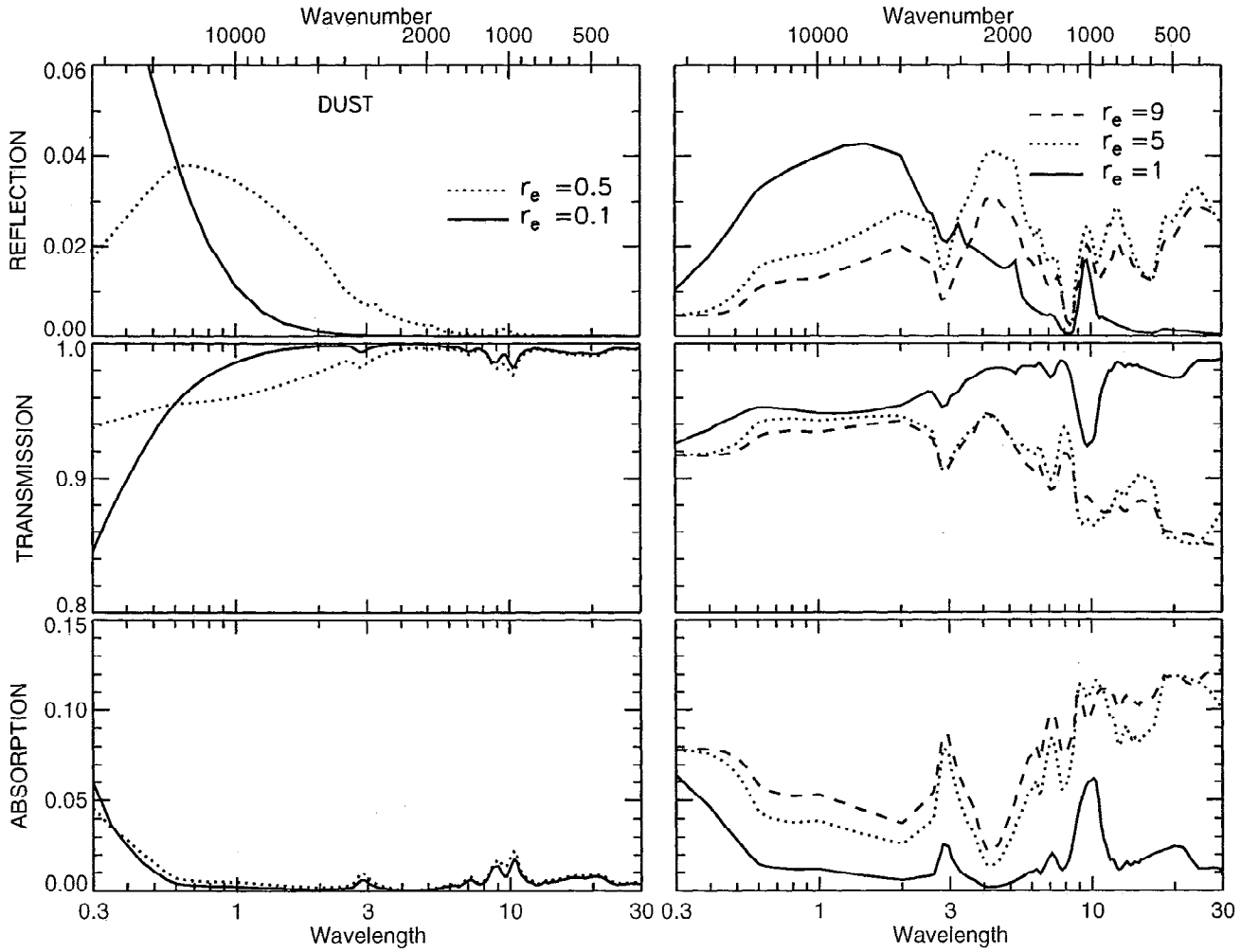

Figure 2. Globally integrated radiative properties for desert dust aerosol for eight particle sizes (effective radii, r_e given in micrometers) in dependence on wavelength (in micrometers).

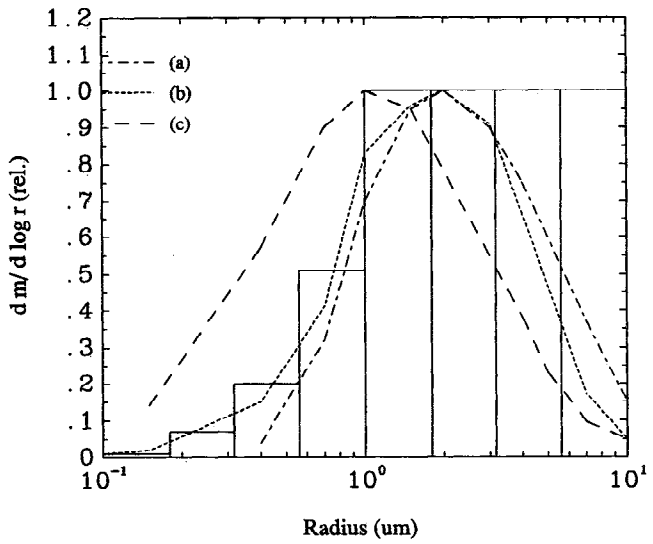

Figure 3. Parameterization of mass size distribution of model dust source (histogram) compared with measurements of mass size distributions (in relative units) above the surface: (a) from *Patterson and Gillette* [1977], (b) from *d'Almeida and Schütz* [1983], and (c) from *Gomes et al.* [1990].

of $\tau = 0.1$ as a function of particle size for three different vertical distributions of dust. Negative flux change stands for an increase in outgoing radiation (primarily solar) and thus implies cooling of the global surface

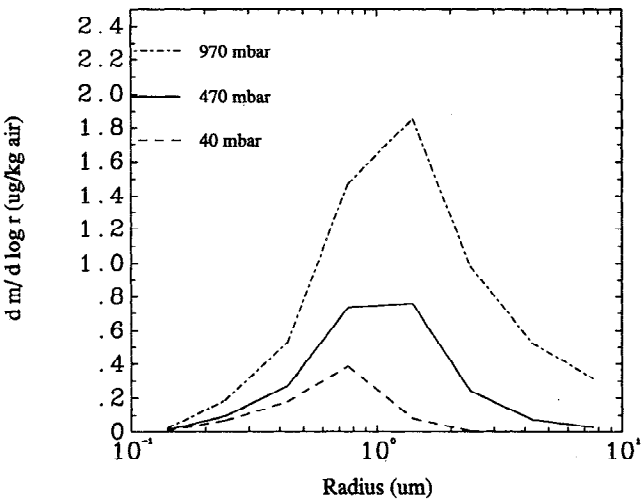

Figure 4. Change of modeled dust size distribution with height.

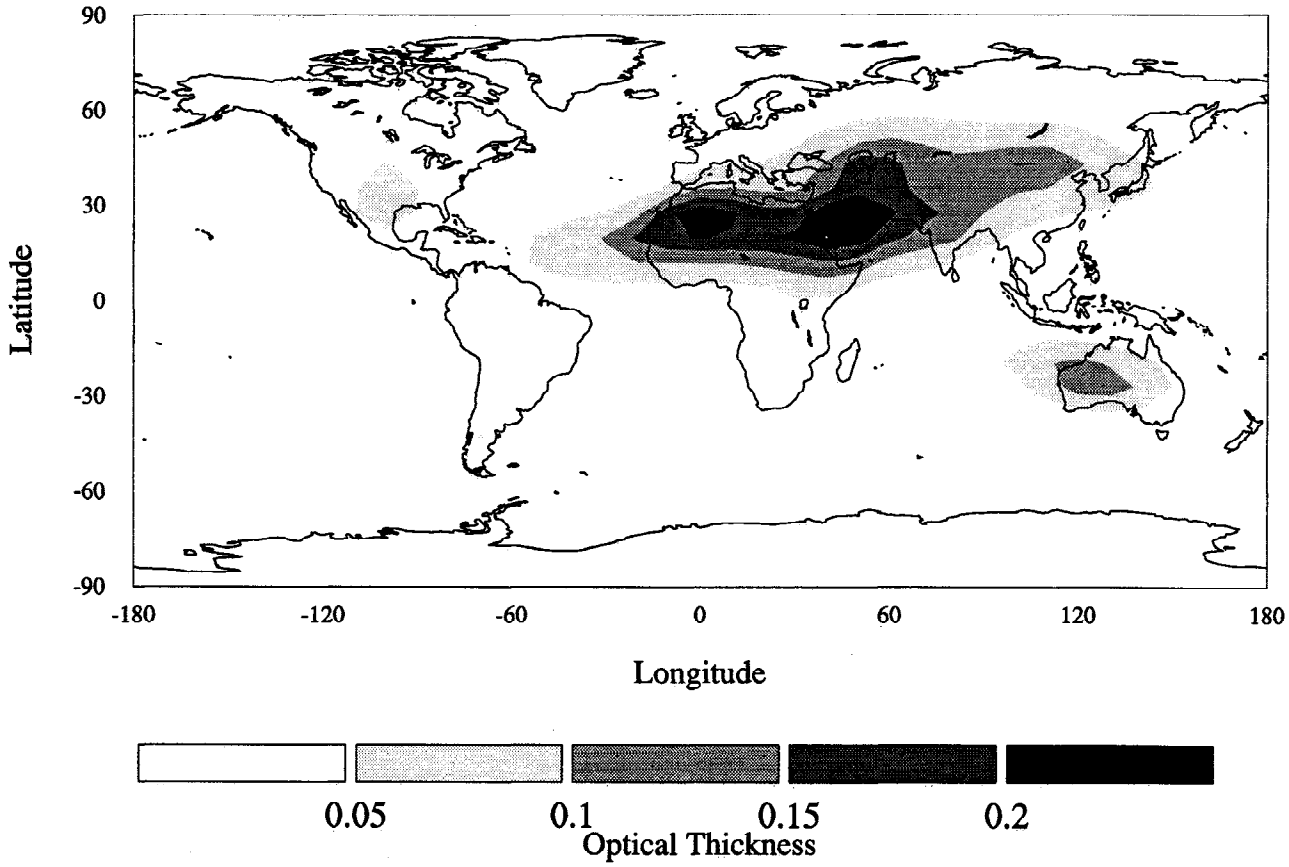

Figure 5. Modeled annual mean dust optical thickness.

temperature. The size and height dependence of the radiative forcing by dust aerosols is shown for a homogeneously mixed dust layer at a height of 0–1 km, 0–3 km, and 3–6 km, respectively. Particles that are smaller than a critical radius (indicated by the dashed vertical lines) produce a negative flux change, and thus cause cooling, because for these sizes the reduction in incident solar radiation exceeds the absorption of thermal radiation (greenhouse effect). Particle sizes larger than the critical radius lead to a positive forcing due to their higher absorption of solar radiation and larger greenhouse effect. The magnitude of the greenhouse forcing depends on the height distribution of the dust, with the critical radius ranging from 1 μm for a dust layer at a height of 3–6 km to 4.7 μm for dust restricted to a layer from 0 to 1 km. This is because the greenhouse effect is smaller when the dust is located closer to the surface. For a dust layer at a height of 0–3 km (which might be the most representative case), the critical particle radius that determines whether the radiative forcing is positive or negative is about 1.8 μm.

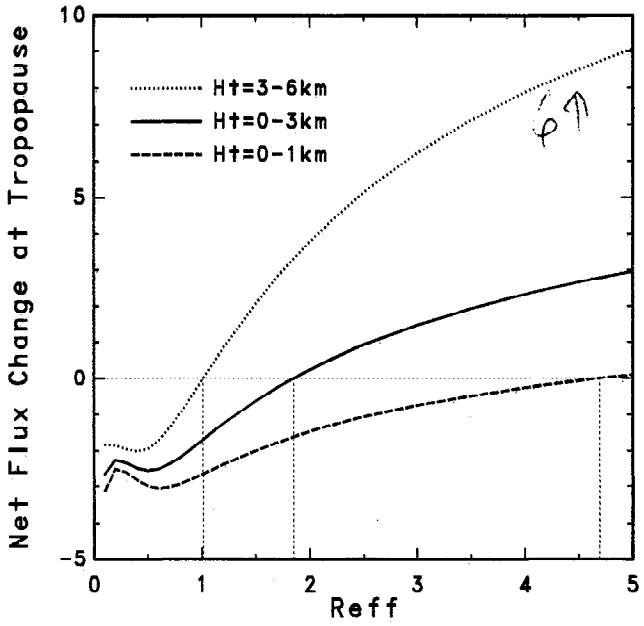

Figure 6. Net change in radiative flux at the tropopause (watts per square meter) for dust optical thickness $\tau = 0.1$ as a function of effective radius (micrometer) for different height distributions.

These results underscore the need for accurate modeling of horizontal and vertical dust distributions and particle size distributions in order to calculate the radiative and climate effects of desert dust, since even the sign of the response depends on the effective particle size and the height distribution of the aerosol.

For a preliminary assessment of the climate impact of the spatial and temporal variability of the radiative forcing by desert dust, we used the radiative code of the 8° × 10° GISS GCM [*Tegen and Lacis,* 1994]. For these first experiments only one "clay" and one "silt" class were considered, with the calculations performed for effective particle sizes of about 0.5 and 2 μm, respectively.

To obtain a measure of the instantaneous radiative forcing by the dust, the model was run with prescribed sea surface temperature but without allowing the effects of aerosol heating to influence the cloud cover and model winds. The results for a 1-year run were then differenced against unforced control run results. On the basis of these calculations, the desert dust was found to cause a global albedo decrease due to the increased absorption at solar wavelengths. The effect is largest in areas with a high dust loading; particularly, the Sahara, the Arabian Peninsula, the Central Asian deserts, northern China and Australia. The calculated regional maximum changes in net radiative flux at the top of the atmosphere are about $+15\,\mathrm{W\,m^{-2}}$ at solar and $+5\,\mathrm{W\,m^{-2}}$ at thermal wavelengths in the annual mean.

A more complete evaluation of the dust effects on climate requires running the GCM with interactive feedbacks allowing for changes in cloud cover and atmospheric dynamics. Initial results with the $8° \times 10°$ GISS GCM suggest that the additional atmospheric heating tends to generate greater stability above dust loaded regions.

6. Conclusions

To calculate the radiative effects and climate impact of desert dust aerosols realistically, an accurate parameterization of dust particle size distribution is necessary, since even the sign of the radiative effect depends on the size of the aerosol. It is found that the essential characteristics of the desert dust transport can be reproduced using eight different particle size classes as individual tracers, spanning the range between 0.1 and $10\,\mu$m radius. As the size classes are transported individually, changes in the mass size distribution of each category can be described by the model. Gravitational sedimentation and rainout are the principal loss mechanisms. Processes like coagulation or destruction of agglomerates which also could cause a change in dust size distribution, were not considered since observational constraints on such processes are not available.

While the column mass load is mainly determined by particles in the size range of 0.6 to $1.8\,\mu$m, the optical thicknesses are mainly determined by particles in the size range between 0.3 and $1\,\mu$m. The contribution of particles larger than $10\,\mu$m to the dust optical thickness can be neglected.

So far, radiative transfer calculations with the GISS GCM have been carried out using two particle size categories. In future experiments, the eight size classes that are described above will be included in the radiation calculations. It is expected that this new parameterization will provide a more realistic representation of the radiative effects of desert dust. The sensitivity of the radiative effects on the aerosol size distribution will be investigated.

Acknowledgments. This work was supported by the NASA Earth Observing Systems (EOS) program.

References

Bouwman, A. F., I. Fung, E. Matthews, and J. John, Global analysis of the potential for N_2O production in natural soils, *Global Biogeochem. Cycles*, *7*, 557–579, 1993.

Coakley, J. A., Jr., and R. D. C. Cess, Response of the NCAR Community Climate Model to the radiative forcing by the naturally occurring tropospheric aerosol, *J. Atmos. Sci.*, *42*, 1677–1692, 1985.

d'Almeida, G., On the variability of desert aerosol characteristics, *J. Geophys. Res.*, *92*, 3017–3026, 1987.

d'Almeida, G., and L. Schütz, Number, mass, and volume distribution of mineral aerosol and soils of the Sahara, *J. Clim. Appl. Meteorol.*, *22*, 233–243, 1983.

Fung, I., K. Prentice, E. Matthews, and G. Russell, Three–dimensional tracer model study of atmospheric CO_2: Response to seasonal exchanges with the terrestrial biosphere, *J. Geophys. Res.*, *88*, 1281–1294, 1983.

Genthon, C., Simulations of desert dust and sea salt aerosols in Antarctica with a general circulation model of the atmosphere, *Tellus*, *44*, 371–389, 1992.

Gillette, D., A wind tunnel simulation of the erosion of soil: Effect of soil texture, sandblasting, wind speed, and soil consolidation on dust production, *Atmos. Environ.*, *12*, 1735–1743, 1978.

Gomes, L., G. Bergametti, G. Coudé-Gaussen, and P. Rognon, Submicron desert dust: A sandblasting process, *J. Geophys. Res.*, *95*, 13,927–13,935, 1990.

Hansen, J. E., and L. D. Travis, Light scattering in planetary atmospheres, *Space Sci. Rev.*, *16*, 527–610, 1974.

Kalma, J. D., J. G. Speight, and R. J. Wasson, Potential wind erosion in Australia: A continental perspective, *J. Clima.*, *8*, 411–428, 1988.

Lacis, A. A., and J. E. Hansen, Parameterization for the absorption of solar radiation in the Earth's atmosphere, *J. Atmos. Sci*, *31*, 118–133, 1974.

Lacis, A. A., and M. I. Mishchenko, Climate forcing, climate sensitivity, and climate response: A radiative modeling perspective on atmospheric aerosols, in *Aerosol Forcing of Climate*, edited by R. Charlson, and J. Heintzenberg, pp. 11–42, John Wiley, New York, 1995.

Matthews, E., New high–resolution data sets for climate studies, *J. Climate Appl. Meteor.*, *22*, 474–487, 1983.

Mishchenko, M. I., Light scattering by size-shape distributions of randomly oriented axially symmetric particles of a size comparable to a wavelength, *Appl. Opt.*, *32*, 4652–4666, 1993.

Mishchenko, M. I., and L. D. Travis, Light scattering by polydispersions of randomly oriented spheroids with sizes comparable to wavelengths of observation, *Appl. Opt.*, *33*, 7206–7225, 1994.

Nakajima, T., M. Tanaka, M. Yamano, M. Shiobara, K. Arao, and Y. Nakanishi, Aerosol optical characteristics in the yellow sand events observed in May, 1982 at Nagasaki. Part 2. Model, *J. Meteorol. Soc. Jpn.*, *67*, 279–291, 1989.

Patterson, E., and D. Gillette, Commonalities in measured size distributions for aerosols having a soil-

derived component, *J. Geophys. Res.*, *82*, 2074–2082, 1977.

Patterson, E. M., D. A. Gillette, and B. H. Stockton, Complex index of refraction between 300 and 700 nm for Saharan aerosols, *J. Geophys. Res.*, *82*, 3153–3160, 1977.

Prather, M. J., B. McElroy, S. C. Wofsy, G. R. Russell, and D. Rind, Chemistry of the global troposphere: Fluorocarbons as tracers of air motion, *J. Geophys. Res.*, *92*, 6579–6613, 1987.

Rao, C. R. N., L. L. Stowe, E. P. McClain, J. Sapper, and M. P. McCormick, Development and application of aerosol remote sensing with AVHRR data from the NOAA satellites, in *Aerosols and Climate*, edited by P. V. Hobbs, A. Deepak, Hampton, Va., 1988.

Scheffer, F., and P. Schachtschabel, *Lehrbuch der Bodenkunde*. 13 ed., F. Enke Verlag, Frankfurt, Germany, 1992.

Shea, D., Climatological atlas: 1950–1979, surface air temperature, precipitation, sea level pressure, and sea surface temperature, Tech. Rep. *NCAR/TN-269+STR*, Natl. Cent. for Atmos. Res., Boulder, Co., 1986.

Tegen, I., and I. Fung, Modeling of mineral dust in the atmosphere: Sources, transport and optical thickness, *J. Geophys. Res.*, *99*, 22,897–22,914, 1994.

Tegen, I., and A. A. Lacis, GCM modeling of the climate impact of desert dust aerosols, in *Eighth Conference on Atmospheric Radiation*, pp. 113–115, Am. Meteorol. Soc, Nashville, Tenn., 1994.

Volz, F. E., Infrared optical constants of ammonium sulfate, Sahara dust, volcanic pumice, and flyash, *Appl. Optics*, *12*, 564–568, 1973.

Zobler, L., A world file for global climate modeling, Tech. Rep. *NASA-TM-87802*, 32 pp., 1986.

Andrew A. Lacis, NASA–Goddard Institute for Space Studies, 2880 Broadway, New York, NY 10025, (e-mail: ccaal@giss.nasa.gov)

Ina Tegen, NASA–Goddard Institute for Space Studies, 2880 Broadway, New York, NY 10025. (e-mail: cxixt@giss.nasa.gov)

(Received March 30, 1995; revised October 8, 1995; accepted November 10, 1995.)